J. Fluid Mech. (2009), *vol.* 627, *pp.* 33–53.
doi:10.1017/S0022112009006028 Printed in the United Kingdom

An exact Riemann-solver-based solution for regular shock refraction

P. DELMONT[1,2]†, R. KEPPENS[1,2,3,4] AND B. VAN DER HOLST[5]

[1]Centre for Plasma Astrophysics, K.U. Leuven, 3001 Heverlee, Belgium

[2]Leuven Mathematical Modeling and Computational Science Centre, 3001 Heverlee, Belgium

[3]Astronomical Institute, Utrecht University, 3584 Utrecht, The Netherlands

[4]FOM institute for Plasma Physics Rijnhuizen, 3434 Nieuwegein, The Netherlands

[5]Centre for Space Environment Modeling, Ann Arbor, MI 48103, USA

(Received 12 August 2008 and in revised form 5 January 2009)

We study the classical problem of planar shock refraction at an oblique density discontinuity, separating two gases at rest. When the shock impinges on the density discontinuity, it refracts, and in the hydrodynamical case three signals arise. Regular refraction means that these signals meet at a single point, called the *triple point*. After reflection from the top wall, the contact discontinuity becomes unstable due to local Kelvin–Helmholtz instability, causing the contact surface to roll up and develop the Richtmyer–Meshkov instability (RMI). We present an exact Riemann-solver-based solution strategy to describe the initial self-similar refraction phase, by which we can quantify the vorticity deposited on the contact interface. We investigate the effect of a perpendicular magnetic field and quantify how its addition increases the deposition of vorticity on the contact interface slightly under constant Atwood number. We predict wave-pattern transitions, in agreement with experiments, von Neumann shock refraction theory and numerical simulations performed with the grid-adaptive code AMRVAC. These simulations also describe the later phase of the RMI.

1. Introduction

We study the classical problem of regular refraction of a shock at an oblique density discontinuity. Long ago, von Neumann (1943) deduced the critical angles for regularity of the refraction, while Taub (1947) found relations between the angles of refraction. Later on, Henderson (1966) extended this work to irregular refraction by use of polar diagrams. An example of an early shock-tube experiment was performed by Jahn (1956). Amongst many others, Abd-El-Fattah & Henderson (1978*a*, *b*) performed experiments in which also irregular refraction occurred.

In 1960, Richtmyer performed the linear stability analysis of the interaction of shock waves with density discontinuities and concluded that the shock-accelerated contact is unstable to perturbations of all wavelengths, for *fast–slow* interfaces. In hydrodynamics (HD) an interface is said to be fast–slow if $\eta > 1$, where η is the density ratio across the interface (figure 1), and slow–fast otherwise. The instability is not a classical fluid instability in the sense that the perturbations grow linearly

† Email address for correspondence: peter.delmont@wis.kuleuven.be

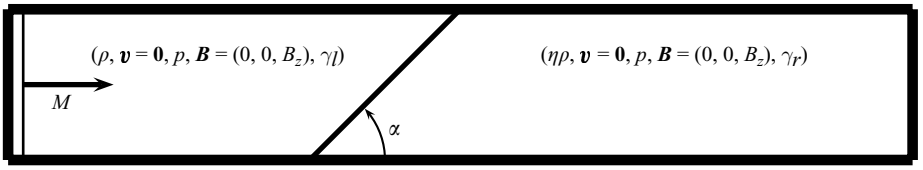

FIGURE 1. Initial configuration: a shock moves with shock speed M to an inclined density discontinuity. Both the upper and lower boundary are solid walls, while the left and the right boundaries are open.

and not exponentially. The first experimental validation was performed by Meshkov (1969). On the other hand, according to linear analysis the interface remains stable for slow–fast interfaces. This misleading result is only valid in the linear phase of the process and near the triple point: a wide range of experimental (e.g. Abd-El-Fattah & Henderson 1978*b*) and numerical (e.g. Nouragliev *et al.* 2005) results show that also in this case the interface becomes unstable. The growth rates obtained by linear theory compare poorly to experimentally determined growth rates (Sturtevant 1987). The governing instability is referred to as the Richtmyer–Meshkov instability (RMI) and is nowadays a topic of research in inertial confinement fusion (e.g. Oron *et al.* 1999), astrophysics (e.g. Kifonidis *et al.* 2006) and the like, and it is a common test problem for numerical codes (e.g. van der Holst & Keppens 2007).

In essence, the RMI is a local Kelvin–Helmholtz instability, due to the deposition of vorticity on the shocked contact. Hawley & Zabusky (1989) formulated an interesting vortex paradigm, which describes the process of shock refraction, using vorticity as the central concept. Later on, Samtaney, Ray & Zabusky (1998) performed an extensive analysis of the baroclinic circulation generation on shocked slow–fast interfaces.

A wide range of fields in which the RMI occurs involves ionized, quasi-neutral plasmas, where the magnetic field plays an important role. Therefore, more recently there has been some research done on the RMI in magnetohydrodynamics (MHD). Samtaney (2003) proved by numerical simulations, exploiting adaptive mesh refinement (AMR), that the RMI is suppressed in planar MHD, when the initial magnetic field is normal to the shock. Wheatley, Pullin & Samtaney (2005) solved the problem of planar shock refraction analytically, making initial guesses for the refracted angles. The basic idea is that ideal MHD does not allow for a jump in tangential velocity, if the magnetic-field component normal to the contact discontinuity (CD) does not vanish (see e.g. Goedbloed & Poedts 2004). The solution of the Riemann problem in ideal MHD is well studied in the literature (e.g. Lax 1957), and due to the existence of three (slow, Alfvén, fast) wave signals instead of one (sound) signal, it is much richer than the HD case. The Riemann problem usually considers the self-similar temporal evolution of an initial discontinuity, while we will consider stationary two-dimensional conditions. The interaction of small perturbations with MHD (switch-on and switch-off) shocks was studied both analytically by Todd (1965) and numerically by Chu & Taussig (1967). Later on, the evolutionarity of intermediate shocks, which cross the Alfvén speed, has been studied extensively. Intermediate shocks are unstable under small perturbations and are thus not evolutionary. Brio & Wu (1988) and De Sterck, Low & Poedts (1998) found intermediate shocks in respectively one- and two-dimensional simulations. The evolutionary condition became controversial, and amongst others Myong & Roe (1997*a*, *b*) have argued that the evolutionary condition is not relevant in dissipative MHD. Chao *et al.* (1993) reported a $2 \rightarrow 4$ intermediate shock observed by *Voyager 1* in 1980, and Feng & Wang (2008) recognized a $2 \rightarrow 3$

intermediate shock, which was observed by *Voyager 2* in 1979. On the other hand, Barmin, Kulikovskiy & Pogorelov (1996) argue that if the full set of MHD equations is used to solve planar MHD, a small tangential disturbance on the magnetic-field vector splits the rotational jump from the compound wave, transforming it into a slow shock. They investigate the reconstruction process of the non-evolutionary compound wave into evolutionary shocks. Also Falle & Komissarov (1997, 2001) do not reject the evolutionary condition and develop a shock-capturing scheme for evolutionary solutions in MHD, However, since all the signals in this paper are essentially hydrodynamical, we do not have to worry about evolutionarity for the set-up considered here.

In this paper, we solve the problem of regular shock refraction exactly, by developing a stationary two-dimensional Riemann solver. Since a normal component of the magnetic field suppresses the RMI, we investigate the effect of a perpendicular magnetic field. The transition from slow–fast to fast–slow refraction is described in a natural way, and the method can predict wave-pattern transitions. We also perform numerical simulations using the grid-adaptive code AMRVAC (Keppens *et al.* 2003; van der Holst & Keppens 2007).

In § 2, we formulate the problem and introduce the governing MHD equations. In § 3, we present our Riemann-solver-based solution strategy, and in § 4, more details on the numerical implementation are described. Finally, in § 5, we present our results, including a case study, the prediction of wave-pattern transitions, comparison to experiments and numerical simulations and the effect of a perpendicular magnetic field on the stability of the CD.

2. Configuration and governing equations

2.1. *Problem set-up*

As indicated in figure 1, the hydrodynamical problem of regular shock refraction is parameterized by five independent initial parameters: the angle α between the shock normal and the initial density discontinuity CD, the sonic Mach number M of the impinging shock, the density ratio η across the CD and the ratios of specific heat γ_l and γ_r on both sides of the CD. The shock refracts in three signals: a reflected signal (R), a transmitted signal (T) and a shocked CD, where we allow both R and T to be expansion fans or shocks. Adding a perpendicular magnetic field B also introduces the plasma-β in the pre-shock region,

$$\beta = \frac{2p}{B^2}, \tag{2.1}$$

which is in our set-up a sixth independent parameter. As argued later, the shock then still refracts in three signals (see figure 3), where we allow both R and T to be expansion fans or shocks.

2.2. *Stationary MHD equations*

In order to describe the dynamical behaviour of ionized, quasi-neutral plasmas, we use the framework of ideal MHD. We thereby neglect viscosity and resistivity and suppose that the length scales of interest are much larger than the Debye length and that there are enough particles in a Debye sphere (see e.g. Goedbloed & Poedts 2004). As written out in conservative form and for our planar problem, the stationary MHD equations are

$$\frac{\partial}{\partial x}\boldsymbol{F} + \frac{\partial}{\partial y}\boldsymbol{G} = 0, \tag{2.2}$$

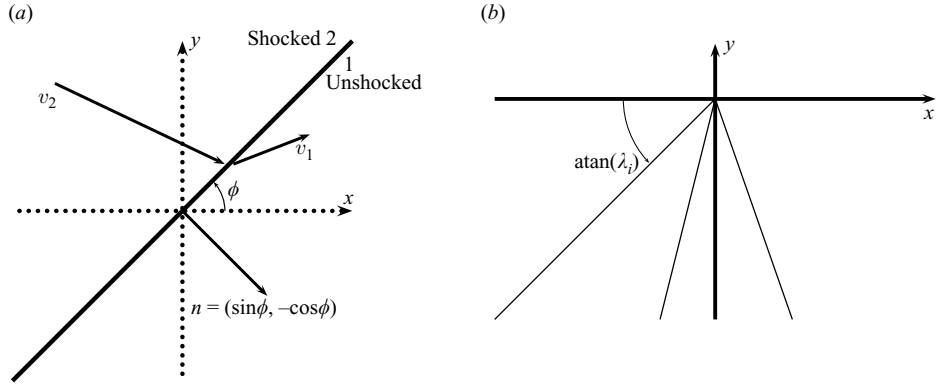

FIGURE 2. (*a*) A stationary shock, separating two constant states across an inclined planar discontinuity. (*b*) The eigenvalues of the matrix $\boldsymbol{A}$ from (3.12) correspond to the refracted signals.

where we introduced the flux terms

$$\boldsymbol{F} = \left(\rho v_x,\, \rho v_x^2 + p + \frac{B^2}{2},\, \rho v_x v_y,\, v_x \left(\frac{\gamma}{\gamma - 1} p + \rho \frac{v_x^2 + v_y^2}{2} + B^2 \right),\, v_x B,\, v_x \gamma \rho \right)^t \tag{2.3}$$

and

$$\boldsymbol{G} = \left(\rho v_y,\, \rho v_x v_y,\, \rho v_y^2 + p + \frac{B^2}{2},\, v_y \left(\frac{\gamma}{\gamma - 1} p + \rho \frac{v_x^2 + v_y^2}{2} + B^2 \right),\, v_y B,\, v_y \gamma \rho \right)^t . \tag{2.4}$$

The applied magnetic field $\boldsymbol{B} = (0, 0, B)$ is assumed purely perpendicular to the flow and the velocity $\boldsymbol{v} = (v_x, v_y, 0)$. Note that the ratio of specific heats γ is interpreted as a variable rather than as an equation parameter, which is done to treat gases and plasmas in a simple analytical and numerical way. The latter equation of the system expresses that $\nabla \cdot (\gamma \rho \boldsymbol{v}) = 0$. Also note that $\nabla \cdot \boldsymbol{B} = 0$ is trivially satisfied.

2.3. *Planar stationary Rankine–Hugoniot condition*

We allow weak solutions of the system, which are solutions of the integral form of the MHD equations. The shock occurring in the problem set-up, as well as those that later on may appear as R or T signals obey the Rankine–Hugoniot conditions. In the case of two-dimensional stationary flows (see figure 2), where the shock speed $s = 0$, the Rankine–Hugoniot conditions follow from (2.2). When considering a thin continuous transition layer in between the two regions, with thickness δ, solutions of the integral form of (2.2) should satisfy $\lim_{\delta \to 0} \int_1^2 ((\partial/\partial x)\boldsymbol{F} + (\partial/\partial y)\boldsymbol{G})\, \mathrm{d}l = 0$. For vanishing thickness of the transition layer this yields the Rankine–Hugoniot conditions as

$$-\lim_{\delta \to 0} \int_1^2 \left(\frac{1}{\sin\phi} \frac{\partial}{\partial l} \boldsymbol{F} - \frac{1}{\cos\phi} \frac{\partial}{\partial l} \boldsymbol{G} \right) \mathrm{d}l = 0 \tag{2.5}$$

$$\Updownarrow$$

$$[[\boldsymbol{F}]] = \xi\, [[\boldsymbol{G}]]\,, \tag{2.6}$$

where $\xi = \tan\phi$ and ϕ is the angle between the x-axis and the shock as indicated in figure 2. The symbol [[ ]] indicates the jump across the interface.

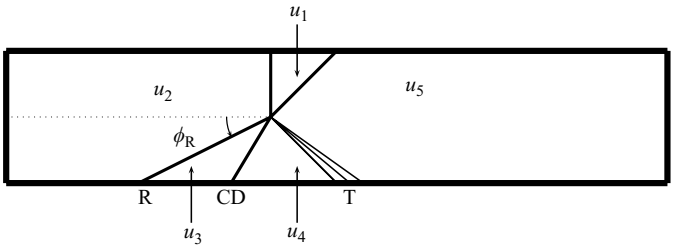

FIGURE 3. The wave pattern during interaction of the shock with the CD. The upper and lower boundaries are rigid walls, while the left and right boundaries are open.

3. Riemann-solver-based solution strategy

3.1. *Dimensionless representation*

In this section we present how we initialize the problem in a dimensionless manner. In the initial refraction phase, the shock will introduce three wave signals (R, CD, T), and two new constant states develop, as schematically shown in figure 3. We choose a representation in which the initial shock speed, s, equals its sonic Mach number, M. We determine the value of the primitive variables in the post-shock region by applying the stationary Rankine–Hugoniot conditions in the shock rest frame. In absence of a magnetic field, we use a slightly different way to non-dimensionalize the problem. Note $\boldsymbol{u_i} = (\rho_i, v_{x,i}, v_{y,i}, p_{tot,i}, B_i, \gamma_i)$, where the index i refers to the value taken in the ith region (figure 3) and the total pressure

$$p_{tot} = p + \frac{B^2}{2}. \tag{3.1}$$

In the HD case, we define $p = 1$ and $\rho = \gamma_l$ in $\boldsymbol{u}_1$. Now all velocity components are scaled with respect to the sound speed in this region between the impinging shock and the initial CD. Since this region is initially at rest, the sonic Mach number, M, of the shock equals its shock speed, s. When the shock intersects the CD, the triple point follows the unshocked contact slip line. It does so at a speed $\boldsymbol{v}_{tp} = (M, M\tan\alpha)$. Therefore we will solve the problem in the frame of the stationary triple point. We will look for self-similar solutions in the frame $\boldsymbol{u} = \boldsymbol{u}(\phi)$, where all signals are stationary. We now have that $\tilde{v}_x = v_x - M$ and $\tilde{v}_y = v_y - M\tan\alpha$, where $\tilde{v}$ refers to this new frame. From now on we will drop the tilde and only use this new frame. We now have $\boldsymbol{u}_1 = (\gamma_l, -M, -M\tan\alpha, 1, 0, \gamma_l)^t$ and $\boldsymbol{u}_5 = (\eta\gamma_l, -M, -M\tan\alpha, 1, 0, \gamma_r)^t$. The Rankine–Hugoniot relations now immediately give a unique solution for $\boldsymbol{u}_2$, namely

$$\boldsymbol{u}_2 = \left(\frac{(\gamma_l^2 + \gamma_l)M^2}{(\gamma_l - 1)M^2 + 2}, -\frac{(\gamma_l - 1)M^2 + 2}{(\gamma_l + 1)M}, -M\tan\alpha, \frac{2\gamma_l M^2 - \gamma_l + 1}{\gamma_l + 1}, 0, \gamma_l \right)^t. \tag{3.2}$$

In MHD, we non-dimensionalize by defining $B = 1$ and $\rho = \gamma_l\beta/2$, in region 1. Again all velocity components are scaled with respect to the sound speed in this region. We now have that $\boldsymbol{u}_1 = (\gamma_l\beta/2, -M, -M\tan\alpha, (\beta+1)/2, 1, \gamma_l)^t$, and from the definition of η, $\boldsymbol{u}_5 = (\eta\gamma_l\beta/2, -M, -M\tan\alpha, (\beta+1)/2, 1, \gamma_r)^t$. The Rankine–Hugoniot relations now give the following non-trivial solutions for $\boldsymbol{u}_2$:

$$\boldsymbol{u}_2 = \left(\frac{-\gamma_l\beta M}{2\omega}, \omega, -M\tan\alpha, p_2 + \frac{M^2}{2\omega^2}, \frac{-M}{\omega}, \gamma_l \right)^t, \tag{3.3}$$

where

$$p_2 = \frac{A\omega + B}{C\omega + D} \tag{3.4}$$

is the thermal pressure in the post-shock region. We introduced the coefficients

$$A = \gamma_l \left(\beta^2\left(4\gamma_l^2 M^4 - 2\gamma_l M^2 - \gamma_l - 1\right) + \beta\left(\left(\gamma_l^2 + 4\gamma_l - 5\right)M^2 - 2\right) - \gamma_l + 2\right), \tag{3.5}$$

$$B = (\gamma_l - 1)M\left(\beta\left(M^2\left(\gamma_l^2 + 7\gamma_l\right) - 2\gamma_l + 4\right) - 2\gamma_l + 4\right), \tag{3.6}$$

$$C = 2\gamma_l(\gamma_l + 1)(\beta((\gamma_l - 1)M^2 + 2) + 2), \tag{3.7}$$

$$D = 4(\gamma_l + 1)(\gamma_l - 2)M. \tag{3.8}$$

The quantity

$$\omega = \omega_{\pm} \equiv -\frac{\gamma_l(\gamma_l - 1)\beta M^2 + 2\gamma_l(\beta + 1) \pm \sqrt{W}}{2\gamma_l(\gamma_l + 1)\beta M}, \tag{3.9}$$

is the normal post-shock velocity relative to the shock, with

$$W = \beta^2 M^2\left(\gamma_l^3 - \gamma_l^2\right)\left(M^2(\gamma_l - 1) + 4\right) + \beta\gamma_l(4M^2\left(4 + \gamma_l - \gamma_l^2\right) + 8\gamma_l) + 4\gamma_l^2. \tag{3.10}$$

Note that ω must satisfy $-M < \omega < 0$ to represent a genuine right-moving shock. We choose the solution in which $\omega = \omega_+$, since the alternative, $\omega = \omega_-$, is a degenerate solution in the sense that the hydrodynamical limit $\lim_{\beta\to+\infty}\omega_- = 0$ does not represent a right-moving shock.

3.2. *Relations across a contact discontinuity and an expansion fan*

Rewriting (2.2) in quasi-linear form leads to

$$\boldsymbol{u}_x + \left(\boldsymbol{F}_{\boldsymbol{u}}^{-1} \cdot \boldsymbol{G}_{\boldsymbol{u}}\right)\boldsymbol{u}_y = \boldsymbol{0}. \tag{3.11}$$

In the frame moving with the triple point, we are searching for self-similar solutions, and we can introduce $\xi = y/x = \tan\phi$, so that $\boldsymbol{u} = \boldsymbol{u}(\xi)$. Assuming that $\xi \mapsto \boldsymbol{u}(\xi)$ is differentiable, manipulating (3.11) leads to $\boldsymbol{A}\boldsymbol{u}_\xi = \xi\boldsymbol{u}_\xi$. So the eigenvalues λ_i of $\boldsymbol{A}$ represent $\tan\phi$, where ϕ is the angle between the refracted signals and the negative x-axis. The matrix $\boldsymbol{A}$ is given by

$$\boldsymbol{A} \equiv \boldsymbol{F}_{\boldsymbol{u}}^{-1}\boldsymbol{G}_{\boldsymbol{u}} = \begin{pmatrix} \frac{v_y}{v_x} & \frac{\rho v_y}{v_x^2 - c^2} & -\frac{\rho v_x}{v_x^2 - c^2} & \frac{v_y}{v_x}\frac{1}{v_x^2 - c^2} & 0 & 0 \\ 0 & \frac{v_x v_y}{v_x^2 - c^2} & -\frac{c^2}{v_x^2 - c^2} & -\frac{v_y}{\rho}\frac{1}{v_x^2 - c^2} & 0 & 0 \\ 0 & 0 & \frac{v_y}{v_x} & \frac{1}{\rho v_x} & 0 & 0 \\ 0 & -\frac{\rho c^2 v_y}{v_x^2 - c^2} & \frac{\rho c^2 v_x}{v_x^2 - c^2} & \frac{v_x v_y}{v_x^2 - c^2} & 0 & 0 \\ 0 & -\frac{B v_y}{v_x^2 - c^2} & -\frac{B v_x}{v_x^2 - c^2} & \frac{v_y}{v_x}\frac{B}{\rho}\frac{1}{v_x^2 - c^2} & \frac{v_y}{v_x} & 0 \\ 0 & 0 & 0 & 0 & 0 & \frac{v_y}{v_x} \end{pmatrix}, \tag{3.12}$$

and its eigenvalues are

$$\lambda_{1,2,3,4,5,6} = \left\{\frac{v_x v_y + c\sqrt{v^2 - c^2}}{v_x^2 - c^2}, \frac{v_y}{v_x}, \frac{v_y}{v_x}, \frac{v_y}{v_x}, \frac{v_y}{v_x}, \frac{v_x v_y - c\sqrt{v^2 - c^2}}{v_x^2 - c^2}\right\}, \tag{3.13}$$

where the magnetosonic speed $c \equiv \sqrt{v_s^2 + v_a^2}$; the sound speed $v_s = \sqrt{\gamma p/\rho}$; and the Alfvén speed $v_a = \sqrt{B^2/\rho}$. Since $\boldsymbol{A}$ has three different eigenvalues, three different signals will arise. When $\boldsymbol{u}_\xi$ exists and $\boldsymbol{u}_\xi \neq 0$, i.e. inside of expansion fans, $\boldsymbol{u}_\xi$ is proportional to a right eigenvector $\boldsymbol{r_i}$ of $\boldsymbol{A}$. Derivation of $\xi = \lambda_i$ with respect to ξ gives $(\nabla_{\boldsymbol{u}} \lambda_i) \cdot \boldsymbol{u}_\lambda = 1$, and thus we find the proportionality constant, giving

$$\boldsymbol{u}_\xi = \frac{\boldsymbol{r_i}}{\nabla_{\boldsymbol{u}} \lambda_i \cdot \boldsymbol{r_i}}. \tag{3.14}$$

While this result assumed continuous functions, we can also mention relations that hold even across discontinuities like the CD. Denoting the ratio $\mathrm{d}\boldsymbol{u_i}/\boldsymbol{r_i} = \kappa$, it follows that $[\boldsymbol{l_i} \cdot \mathrm{d}\boldsymbol{u}]_{\mathrm{d}x = \lambda_j \mathrm{d}y} = (\boldsymbol{l_i} \cdot \boldsymbol{r}_j)\kappa = \kappa \delta_{i,j}$, where $\boldsymbol{l_i}$ and $\boldsymbol{r_i}$ are respectively the left and right eigenvectors corresponding to λ_i. Therefore, if $i \neq j$,

$$[\boldsymbol{l_i} \cdot \mathrm{d}\boldsymbol{u}]_{\mathrm{d}x = \lambda_j \mathrm{d}y} = 0. \tag{3.15}$$

From these general considerations the following relations hold across the contact or shear wave where the ratio $\mathrm{d}y/\mathrm{d}x = v_y/v_x$:

$$\left.\begin{aligned} v_y \,\mathrm{d}v_x - v_x \,\mathrm{d}v_y + \frac{c\sqrt{v^2 - c^2}}{\rho v_s^2} \,\mathrm{d}p_{tot} = 0, \\ v_y \,\mathrm{d}v_x - v_x \,\mathrm{d}v_y - \frac{c\sqrt{v^2 - c^2}}{\rho v_s^2} \,\mathrm{d}p_{tot} = 0. \end{aligned}\right\} \tag{3.16}$$

Since $v \neq c$, otherwise all signals would coincide, it follows immediately that the total pressure, p_{tot}, and the direction of the streamlines v_y/v_x remain constant across the shocked CD.

These relations across the CD allow to solve the full problem using an iterative procedure. Inspired by the exact Riemann solver described in Toro (1999), we first guess the total pressure p^* across the CD; R is a shock when p^* is larger than the post-shock total pressure, and T is a shock only if p^* is larger than the pre-shock total pressure. Note that the jump in tangential velocity across the CD is a function of p^*, and it must vanish. A simple Newton–Raphson iteration on this function $[[v_y/v_x]](p^*)$ finds the correct p^*. We explain further in § 3.5 how we find the functional expression and iterate to eventually quantify ϕ_R, ϕ_T, ϕ_{CD} and the full solution $\boldsymbol{u}(x, y, t)$. From now on p^* represents the constant total pressure across the CD.

Similarly, from the general considerations above, (3.15) gives that along $\mathrm{d}y/\mathrm{d}x = (v_x v_y \pm c\sqrt{v^2 - c^2})/v_x^2 - c^2$ the following relations connect two states across expansion fans:

$$\left.\begin{aligned} \mathrm{d}\rho - \frac{1}{c^2} \,\mathrm{d}p_{tot} = 0, \\ v_x \,\mathrm{d}v_x + v_y \,\mathrm{d}v_y + \frac{c^2}{\rho v_s^2} \,\mathrm{d}p_{tot} = 0, \\ -\rho \,\mathrm{d}p_{tot} + p_{tot} \rho \,\mathrm{d}\gamma + p_{tot} \gamma \,\mathrm{d}\rho = 0, \\ -B \,\mathrm{d}p_{tot} + (\gamma p + B^2) \,\mathrm{d}B = 0, \\ v_y \,\mathrm{d}v_x - v_x \,\mathrm{d}v_y \pm \frac{c\sqrt{v^2 - c^2}}{\rho v_s^2} \,\mathrm{d}p_{tot} = 0. \end{aligned}\right\} \tag{3.17}$$

These can be written in a form which we exploit to numerically integrate the solution through expansion fans, namely

$$\left.\begin{aligned}
\rho_i &= \rho_e + \int_{p_{tot,e}}^{p^*} \frac{1}{c^2}\,\mathrm{d}p_{tot}\,,\\
v_{x,i} &= v_{x,e} + \int_{p_{tot,e}}^{p^*} \frac{\pm v_y\sqrt{v^2-c^2} - v_x c}{\rho v^2 c}\,\mathrm{d}p_{tot}\,,\\
v_{y,i} &= v_{y,e} + \int_{p_{tot,e}}^{p^*} \frac{\mp v_x\sqrt{v^2-c^2} - v_y c}{\rho v^2 c}\,\mathrm{d}p_{tot}\,,\\
B_i &= B_e + \int_{p_{tot,e}}^{p^*} \frac{B}{\rho c^2}\,\mathrm{d}p_{tot}\,,\\
p_i &= p_e + \int_{p_{tot,e}}^{p^*} \frac{v_s^2}{c^2}\,\mathrm{d}p_{tot}\,,\\
\gamma_i &= \gamma_e.
\end{aligned}\right\} \tag{3.18}$$

The indices i and e stand respectively for *internal* and *external*, the states at both sides of the expansion fans. The upper signs hold for reflected expansion fans (i.e. of type R), while the lower sign holds for transmitted expansion fans (i.e. of type T).

3.3. *Relations across a shock*

Since the system is nonlinear and allows for large-amplitude shock waves, the analysis given thus far is not sufficient. We must include the possibility of one or both of the R and T signals to be solutions of the stationary Rankine–Hugoniot conditions (2.6). The solution is given by

$$\left.\begin{aligned}
\rho_i &= \frac{\frac{\gamma-1}{\gamma+1} + \frac{p^*}{p_{tot,e}}}{\frac{\gamma-1}{\gamma+1}\frac{p^*}{p_{tot,e}} + 1}\rho_e,\\
v_{x,i} &= v_{x,e} - \frac{\xi_{\mp}(p^* - p_{tot,e})}{\rho_e(v_{x,e}\xi_{\mp} - v_{y,e})},\\
v_{y,i} &= v_{y,e} + \frac{p^* - p_{tot,e}}{\rho_e(v_{x,e}\xi_{\mp} - v_{y,e})},\\
B_i &= \frac{\frac{\gamma-1}{\gamma+1} + \frac{p^*}{p_{tot,e}}}{\frac{\gamma-1}{\gamma+1}\frac{p^*}{p_{tot,e}} + 1}B_e,\\
\gamma_i &= \gamma_e,\\
p_i &= p^* - \frac{B_i^2}{2},\\
\phi_{R/T} &= \mathrm{atan}(\xi_{+/-}),
\end{aligned}\right\} \tag{3.19}$$

where

$$\xi_{\pm} = \frac{v_{e,x}v_{e,y} \pm \hat{c}_e\sqrt{v_e^2 - \hat{c}_e^2}}{v_{e,x}^2 - \hat{c}_e^2} \tag{3.20}$$

and

$$\hat{c}_e^2 = \frac{(\gamma-1)p_{tot,e} + (\gamma+1)p^*}{2\rho_e}. \tag{3.21}$$

Again the indices i and e stand respectively for *internal* and *external*, the states at both sides of the shocks. The upper signs holds for reflected shocks, while the lower sign holds for transmitted shocks.

3.4. *Shock refraction as a Riemann problem*

We are now ready to formulate our iterative solution strategy. Since there exist two invariants across the CD, it follows that we can do an iteration, if we are able to express one invariant in function of the other. As mentioned earlier, we choose to iterate on $p^* = p_{tot,3} = p_{tot,4}$. This is the only state variable in the solution, and it controls both R and T. We will write $\phi_R = \phi_R(\boldsymbol{u}_2, p*)$ and $\phi_T = \phi_T(\boldsymbol{u}_5, p^*)$, $\boldsymbol{u}_3 = \boldsymbol{u}_3(\boldsymbol{u}_2, p^*)$ and $\boldsymbol{u}_4 = \boldsymbol{u}_4(\boldsymbol{u}_5, p^*)$. The other invariant should match too, i.e. $(v_{x,3}/v_{y,3}) - (v_{x,4}/v_{y,4}) = 0$. Since $\boldsymbol{u}_2$ and $\boldsymbol{u}_5$ only depend on the input parameters, this last expression is a function of p^*. Iteration on p^* gives p^* and $\phi_R = \phi_R(p^*)$, $\phi_T = \phi_T(p^*)$, $\boldsymbol{u}_3 = \boldsymbol{u}_3(p^*)$ and $\boldsymbol{u}_4 = \boldsymbol{u}_4(p^*)$ give $\phi_{CD} = \mathrm{atan}(v_{y,3}/v_{x,3}) = \mathrm{atan}(v_{y,4}/v_{x,4})$, which solves the problem.

3.5. *Solution inside of an expansion fan*

The only ingredient not yet fully specified by our description above is how to determine the variation through possible expansion fans. This can be done once the solution for p^* is iteratively found, by integrating (3.18) till the appropriate value of p_{tot}. Notice that the location of the tail of the expansion fan is found by $\tan(\phi_{tail}) = (v_{y,i} v_{x,i} \pm c_i \sqrt{v_i^2 - c_i^2})/v_{x,i}^2 - c_i^2$, and the position of ϕ_{head} is uniquely determined by $\tan(\phi_{head}) = (v_{y,e} v_{x,e} \pm c_e \sqrt{v_e^2 - c_e^2})/v_{x,e}^2 - c_e^2$. Inside an expansion fan we know $\boldsymbol{u}(p_{tot})$, so now we need to find $p_{tot}(\phi)$, in order to find a solution for $\boldsymbol{u}(\phi)$. We decompose vectors locally in the normal and tangential directions, which are respectively referred to with the indices n and t. We denote taking derivatives with respect to ϕ as $'$. Inside of the expansion fans we have some invariants given by (3.17). The fourth of these immediately leads to p/B^γ as an invariant. Eliminating p_{tot} from $\mathrm{d}\rho - (1/c^2)\,\mathrm{d}p_{tot} = 0$ and $-B\,\mathrm{d}p_{tot} + (\gamma p + B^2)\,\mathrm{d}B = 0$ yields the invariant ρ/B, and combining these two invariants tells us that the entropy $S \equiv p/\rho^\gamma$ is invariant. The stationary MHD equations (2.2) can then be written in a 4×4 system for v_n', v_t', p_{tot}' and ρ' as

$$\left.\begin{aligned} v_n' + v_t + v_n \frac{\rho'}{\rho} &= 0, \\ v_n v_t + v_n v_n' + \frac{p_{tot}'}{\rho} &= 0, \\ v_n^2 - v_n v_t' &= 0, \\ c^2 \rho' - p_{tot}' &= 0, \end{aligned}\right\} \tag{3.22}$$

where we dropped B' from the system, since it is proportional to ρ'. Note that γ' vanishes. The system leads to the dispersion relation

$$v_n^4 - c^2 v_n^2 = 0, \tag{3.23}$$

which in differential form becomes

$$4\rho v_n^3 v_n' + v_n^4 \rho' - \gamma v_n^2 p_{tot}' - 2\gamma p_{tot} v_n v_n' - (2-\gamma) B v_n^2 B' - (2-\gamma) B^2 v_n v_n' = 0. \tag{3.24}$$

Elimination of v_n', ρ' and B' gives

$$\frac{\mathrm{d}p_{tot}}{\mathrm{d}\phi} = 2 \frac{v_t}{v_n} \frac{c^2 - 2v_n^2}{3v_n^2 + (\gamma - 2)c^2} \rho c^2. \tag{3.25}$$

This expression allows us to then complete the exact solution as a function of ϕ.

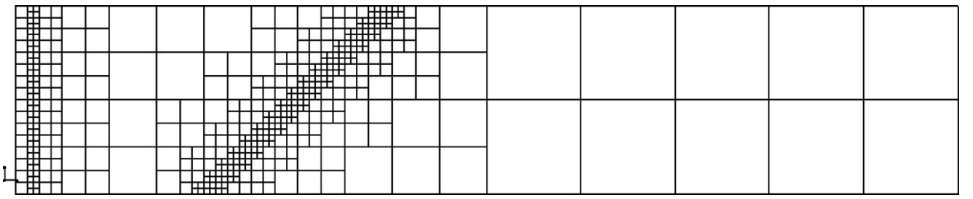

FIGURE 4. The initial AMR grid at $t = 0$, for the example in § 5.1.

4. Implementation and numerical details

4.1. *Details on the Newton–Raphson iteration*

We can generally note that $p_{tot,pre} < p_{tot,post}$. This implies that the refraction has three possible wave configurations: two shocks; a reflected rarefaction fan and a transmitted shock; and two expansion fans. Before starting the iteration on $[[v_y/v_x]](p^*)$, we determine the governing wave configuration. If $[[v_y/v_x]](\epsilon)$ and $[[v_y/v_x]](p_{tot,5} - \epsilon)$ differ in sign, the solution has two rarefaction waves. If $[[v_y/v_x]](p_{tot,5} + \epsilon)$ and $[[v_y/v_x]](p_{tot,2} - \epsilon)$ differ in sign, the solution has a transmitted shock and a reflected rarefaction wave. In the other case, the solution contains two shocks in its configuration. If R is an expansion fan, we take the guess

$$p_0^* = \frac{\min\left\{\dfrac{2\rho_e v_{x,e}^2 - (\gamma_e - 1)p_{tot,e}}{\gamma + 1} | e \in \{2, 5\}\right\} + p_{tot,5}}{2} \tag{4.1}$$

as a starting value of the iteration. This guess is the mean of the critical value $p_{tot,crit}$, which satisfies

$$v_{e,x}^2 - \hat{c}^2(p_{tot,crit}) = 0 \tag{4.2}$$

and p_5, which is the minimal value for a transmitted shock. As we explain in § 5.3, $v_{2,x}^2 - \hat{c}^2(p_{tot,crit}) = 0$ is equivalent to $v_5^2 - \hat{c}^2 = 0$, and $v_{5,x}^2 - \hat{c}^2(p_{tot,crit}) = 0$ is equivalent to $v_2^2 - \hat{c}^2 = 0$ and thus a maximal value for the existence of a regular solution. If R is a shock, we take $(1 + \hat{\epsilon})p_{post}$, where $\hat{\epsilon}$ is 10^{-6}, as a starting value for the iteration. We use a Newton–Raphson interation: $p_{i+1}^* = p_i^* - f(p_i^*)/f'(p_i^*)$, where $f'(p^*)$ is approximated numerically by $(f(p_i^* + \delta) - f(p_i^*))/\delta$, where $\delta = 10^{-8}$. The iteration stops when $(p_{i+1}^* - p_i^*)/p_i^* < \epsilon$, where $\epsilon = 10^{-8}$.

4.2. *Details on AMRVAC*

AMRVAC (Keppens *et al.* 2003; van der Holst & Keppens 2007) is an AMR code, solving equations of the general form $\boldsymbol{u}_t + \nabla \cdot \boldsymbol{F}(u) = \boldsymbol{S}(\boldsymbol{u}, \boldsymbol{x}, t)$ in any dimensionality. The applications cover multi-dimensional HD, MHD, up to special relativistic magnetohydrodynamic computations. In regions of interests, the AMR code dynamically refines the grid. The initial grid of our simulation is shown in figure 4. The refinement strategy is done by quantifying and comparing gradients. The AMR in AMRVAC is of a block-based nature, where every refined grid has 2^D children with D being the dimensionality of the problem. Parallelization is implemented, using Message Passing Interface (MPI). In all the simulations we use five refinement levels, starting with a resolution of 24×120 on the domain $[0, 1] \times [0, 5]$, leading to an effective resolution of 384×1940. The shock is initially located at $x = 0.1$, while the CD is located at $y = (x - 1)\tan\alpha$. We used the fourth-order Runge–Kutta time-stepping, together with a TVDLF scheme (see Yee 1989; Tóth & Odstrčil 1996) with Woodward limiter on the primitive variables. The obtained numerical results were compared to

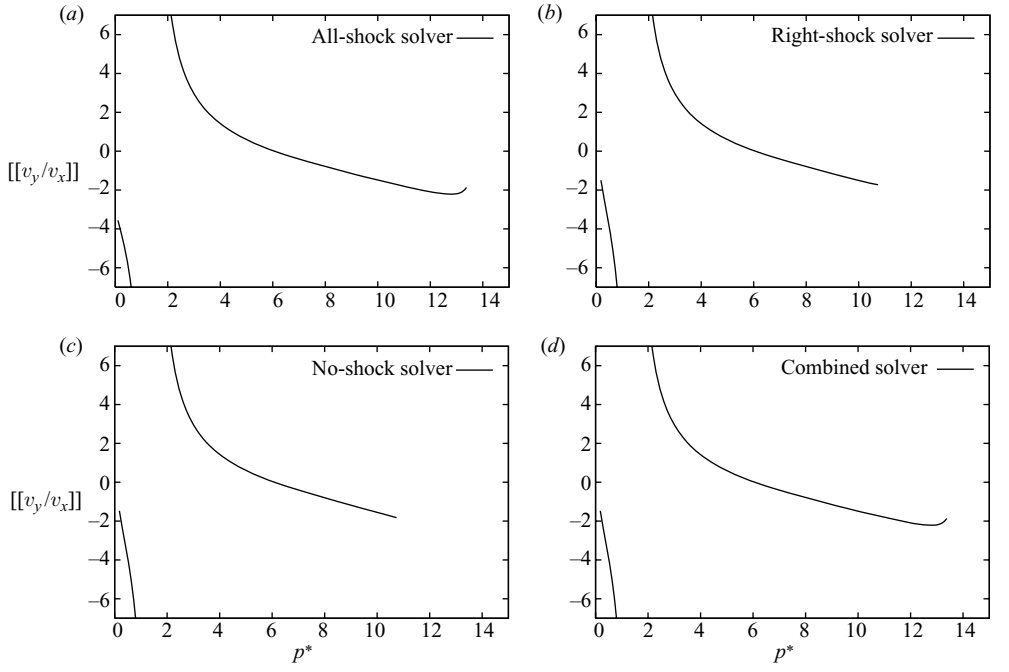

FIGURE 5. For the reference case from Samtaney (2003), $[[v_y/v_x]](p^*)$: (*a*) all-shock solver; (*b*) right-shock solver; (*c*) no-shock solver; (*d*) shock $\Leftrightarrow$ $p^* > p_i$. The all-shock solver is selected.

and in agreement with simulations using other schemes, such as a Roe scheme and the TVD-MUSCL scheme. The calculations were performed on FOUR processors.

4.3. *Following an interface numerically*

The AMRVAC implementation contains slight differences with the theoretical approach. Implementing the equations as we introduced them here would lead to excessive numerical diffusion on γ. Since γ is a discrete variable we know $\gamma(x, y, t)$ exactly, if we are able to follow the CD in time. Suppose thus that initially a surface, separates two regions with different values of γ. Define a function $\chi : D \times \mathbb{R}^+ \to \mathbb{R} : (x, y, t) \mapsto \chi(x, y, t)$, where D is the physical domain of (x, y). Writing $\tilde{\chi}(x, y) = \chi(x, y, 0)$, we ask $\tilde{\chi}$ to vanish on the initial contact and to be a smooth function obeying

(i) $\gamma = \gamma_l \Leftrightarrow \tilde{\chi}(x, y) < 0$,

(ii) $\gamma = \gamma_r \Leftrightarrow \tilde{\chi}(x, y) > 0$.

We take in particular $\pm\tilde{\chi}$ to quantify the shortest distance from the point (x, y) to the initial contact, taking the sign into account. Now we only have to note that $(\chi\rho)_t = \chi\rho_t + \rho\chi_t = -\chi\nabla \cdot (\rho\boldsymbol{v}) - (\rho\boldsymbol{v} \cdot \nabla)\chi = -\nabla \cdot (\chi\rho\boldsymbol{v})$. The implemented system is thus (2.2), but the last equation is replaced by $(\chi\rho v_x)_x + (\chi\rho v_y)_y = 0$. It is now straightforward to show that we did not introduce any new signal. In essence, this is the approach presented in Mulder, Osher & Sethian (1992).

5. Results

5.1. *Fast–slow example solution*

As a first hydrodynamical example, we set $(\alpha, \beta^{-1}, \gamma_l, \gamma_r, \eta, M) = (\pi/4, 0, 7/5, 7/5, 3, 2)$, as originally presented in Samtaney (2003). In figure 5, the first three

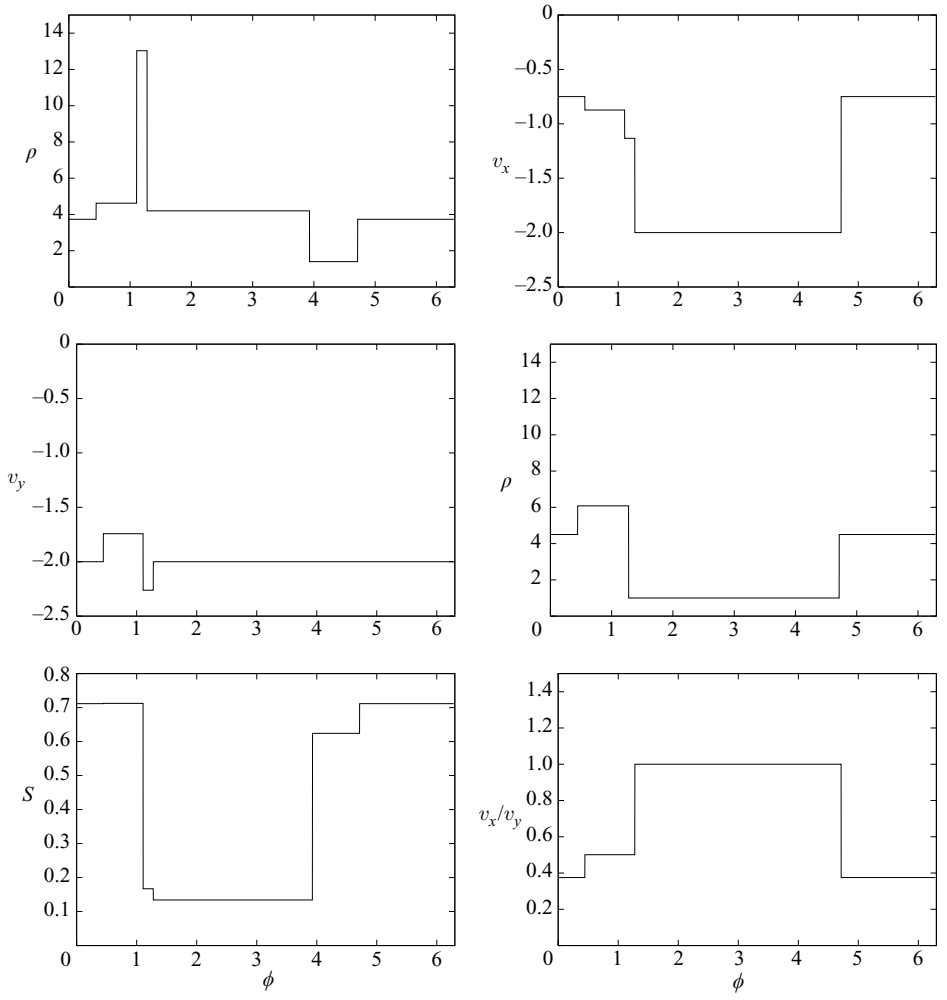

FIGURE 6. Solution to the fast–slow refraction problem, for the reference case from Samtaney (2003). Notice that p and v_x/v_y remain constant across the shocked contact.

plots show $[[v_y/v_x]](p^*)$, when assuming a prescribed wave configuration, for all three possible configurations. The last plot shows the actual function $[[v_y/v_x]](p^*)$, which consists of piecewise copies from the three possible configurations in the previous plots. The initial guess is $p_0^* = 4.111$; the all-shock solver is selected; and the iteration converges after three iterations with $p^* = 6.078$. The full solution of the Riemann problem is shown in figure 6.

5.2. *Slow–fast example*

In figure 7 we show the full solution of the HD Riemann problem, in which the reflected signal is an expansion fan, connected to the refraction with parameters $(\alpha, \beta^{-1}, \gamma_l, \gamma_r, \eta, M) = (\pi/3, 0, 7/5, 7/5, 1/10, 10)$ from van der Holst & Keppens (2007). The refraction is slow–fast, and R is an expansion fan. Note that p and v_y/v_x remain constant across the CD, and the entropy S is an invariant across R.

5.3. *Tracing the critical angle for regular shock refraction*

Let us examine what the effect of the angle of incidence, α, is. Therefore we get back to the example from § 5.1, $(\beta^{-1}, \gamma_l, \gamma_r, \eta, M) = (0, 7/5, 7/5, 3, 2)$, and let

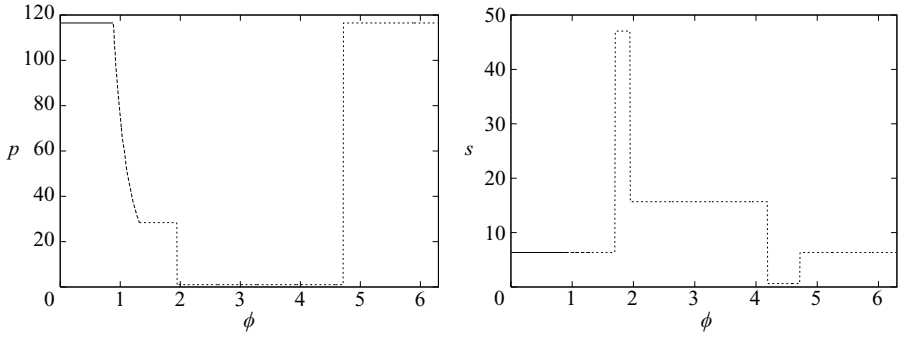

FIGURE 7. Solution to the slow–fast refraction problem from van der Holst & Keppens (2007). Notice that S remains constant across R.

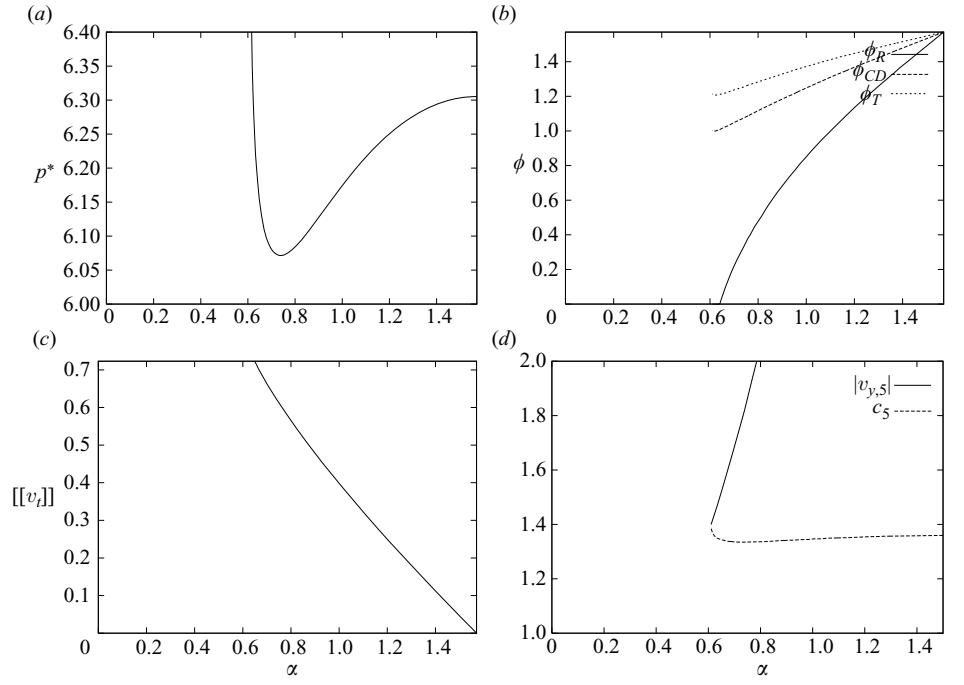

FIGURE 8. (*a*) $p^*(\alpha)$. Note that for $\alpha < 0.61$, there are no solutions for p^*: the refraction is irregular. (*b*) The wave pattern for regular refraction. (*c*) For $\alpha = \pi/2$, the problem is one-dimensional, and there is no vorticity deposited on the interface. For decreasing α, the vorticity increases. (*d*) For regular refraction, $|v_{y,5}| > \hat{c}_5$.

α vary: $\alpha \in]0, \pi/2]$. Note that $\alpha = \pi/2$ corresponds to a one-dimensional Riemann problem. The results are shown in figure 8. Note that for regular refraction $v_{y,5}^2 > \hat{c}_5^2$. We can understand this by noting that $\xi_\pm = (v_{e,x}v_{e,y} \pm \hat{c}_e\sqrt{v_e^2 - \hat{c}_e^2})/v_{e,x}^2 - \hat{c}_e^2 = ((v_{e,x}v_{e,y} \mp \hat{c}_e\sqrt{v_e^2 - \hat{c}_e^2})/v_{e,y}^2 - \hat{c}_e^2)^{-1} = \hat{\xi}_\mp$, which are the eigenvalues of $\boldsymbol{G}_{\boldsymbol{u}}^{-1} \cdot \boldsymbol{F}_{\boldsymbol{u}} = (\boldsymbol{F}_{\boldsymbol{u}}^{-1} \cdot \boldsymbol{G}_{\boldsymbol{u}})^{-1}$. Note that we could have started our theory from the quasi-linear form $\boldsymbol{u}_y + (\boldsymbol{G}_{\boldsymbol{u}}^{-1} \cdot \boldsymbol{F}_{\boldsymbol{u}})\boldsymbol{u}_x = 0$ instead of (3.11). If we would have done so, we would have found eigenvalues $\hat{\xi}$, which would correspond to $1/\text{atan}\phi$. Moreover, both the eigenvalues, ξ_+ and ξ_-, have four singularities, namely $\hat{c}_2 \in \{-v_{x,2}, v_{x,2}, -v_{y,5}, v_{y,5}\}$ for ξ_- and $\hat{c}_5 \in \{-v_{x,5}, v_{x,5}, -v_{y,2}, v_{y,2}\}$ for ξ_+, where thus $\hat{c}_5^2 = v_{5,y}^2 \Leftrightarrow \hat{c}_2^2 = v_2^2$ and

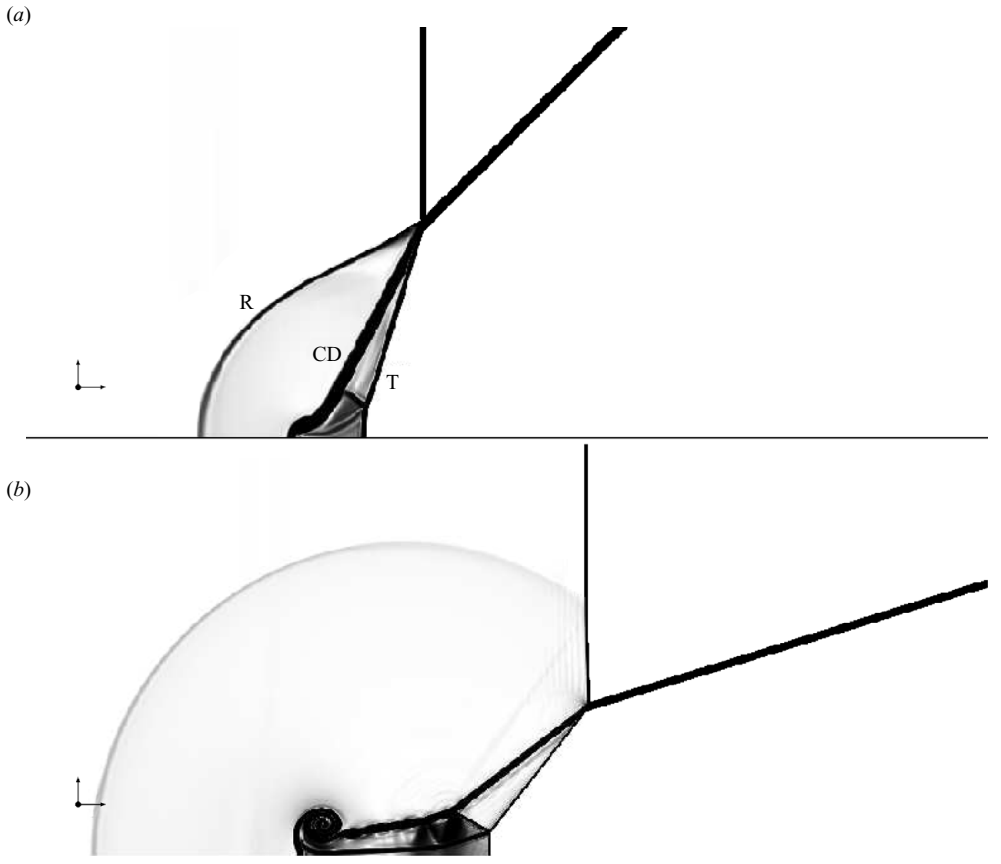

FIGURE 9. Schlieren plots of the density for $(\beta^{-1}, \gamma_l, \gamma_r, \eta, M) = (0, 7/5, 7/5, 3, 2)$ with varying α. (*a*) $\alpha = \pi/4$: a regular reference case. (*b*) $\alpha = 0.3$: an irregular case.

$\hat{c}_2^2 = v_{y,2}^2 \Leftrightarrow \hat{c}_5^2 = v_5^2$. It is now clear that it is one of the latter conditions that will be met for α_{crit}. In the example, the transition to irregular refraction occurs at $-v_{y,5} = \hat{c}_5$ and $\lim_{\alpha \to \alpha_{crit}} p^* = (2\gamma_r \eta M^2 \tan^2(\alpha_{crit}) - \gamma_l + 1)/\gamma_l + 1 = 6.67$. Figure 9 shows Schlieren plots for density from AMRVAC simulations for the reference case $\alpha = \pi/4$, the irregular case and $\alpha = 0.3$. In the regular case, all signals meet at the triple point, while for $\alpha < \alpha_{crit} = 0.61$, the signals do not meet at one triple point; the triple point forms a more complex structure and becomes irregular. The CD, originated at the Mach stem, reaches the triple point through an evanescent wave, which is visible by the contour lines. This pattern is called *Mach reflection–refraction*. Decreasing α even more, the reflected wave transforms in a sequence of weak wavelets (see e.g. Nouragliev *et al.* 2005). This pattern, of which the case $\alpha = 0.3$ is an example, is called *concave-forwards irregular refraction*. These results are in agreement with our predictions.

5.4. *Abd-El-Fattah and Henderson's experiment*

In 1978, a shock-tube experiment was performed by Abd-El-Fattah & Henderson (1978*b*). It became a typical test problem for simulations (see e.g. Nouragliev *et al.* 2005) and refraction theory (see e.g. Henderson 1991). The experiment concerns a slow–fast shock refraction at a CO_2/CH_4 interface. The gas constants are $\gamma_{CO_2} = 1.288$, $\gamma_{CH_4} = 1.303$, $\mu_{CO_2} = 44.01$ and $\mu_{CH_4} = 16.04$. Thus $\eta = \mu_{CH_4}/\mu_{CO_2} = 0.3645$. A very weak shock $M = 1.12$ is refracted at the interface

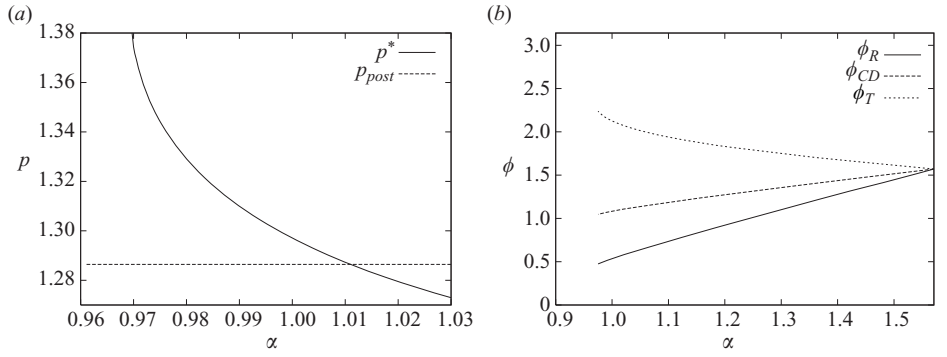

FIGURE 10. Exact solution for the Abd-El-Fattah experiment. (*a*) $p^*(\alpha)$ confirms $\alpha_{crit} = 0.97$ and $\alpha_{trans} = 1.01$. (*b*) $\phi(\alpha)$.

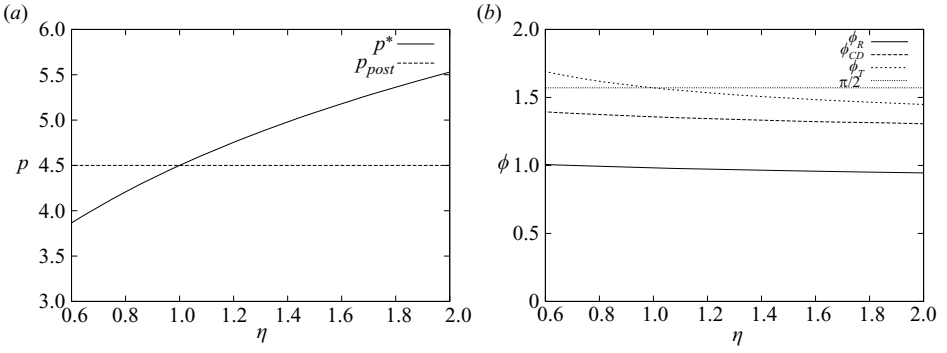

FIGURE 11. Exact solution for $(\alpha, \beta^{-1}, \gamma_l, \gamma_r, M) = (\pi/4, 0, 7/5, 7/5, 2)$ and a varying range of the density ratio η. (*a*) For $\eta < 1$ we have $p^* < p_{post} = 4.5$ and thus a reflected expansion fan; for $\eta > 1$ we have $p^* > p_{post} = 4.5$ and thus a reflected shock. (*b*) For $\eta < 1$, $\phi_T < \pi/2$, and for $\eta > 1$, $\phi_T > \pi/2$.

under various angles. The von Neumann (1943) theory predicts the critical angle $\alpha_{crit} = 0.97$ and the transition angle $\alpha_{trans} = 1.01$, where the reflected signal is irregular if $\alpha < \alpha_{crit}$, a shock if $\alpha_{crit} < \alpha < \alpha_{trans}$ and an expansion fan if $\alpha_{trans} < \alpha$. This is in perfect agreement with the results of our solution strategy as illustrated in figure 10. There we show the pressure p^* compared to the post-shock pressure p_{post}, as well as the angles ϕ_R, ϕ_{CD} and ϕ_T for varying angle of incidence α. Irregular refraction means that not all signals meet at a single point. The transition at α_{crit} is one between a regular shock–shock pattern and an irregular bound precursor refraction, where the transmitted signal is ahead of the shocked contact and moves along the contact at nearly the same velocity. This is also confirmed by AMRVAC simulations. If the angle of incidence, α, is decreased even further, the irregular pattern becomes a free precursor refraction, where the transmitted signal moves faster than the shocked contact, and reflects itself, introducing a side wave, connecting T to CD. When decreasing α even further, another transition to the free precursor von Neumann refraction occurs.

5.5. *Connecting slow–fast to fast–slow refraction*

Another example of how to trace transitions by the use of our solver is done by changing the density ratio η across the CD. Let us start from the example given in § 5.1, and let us vary the value of η.

Here we have $(\alpha, \beta^{-1}, \gamma_l, \gamma_r, M) = (\pi/4, 0, 7/5, 7/5, 2)$. The results are shown in figure 11. Note that, since $p_{post} = 4.5$, we have a reflected expansion fan for fast–slow

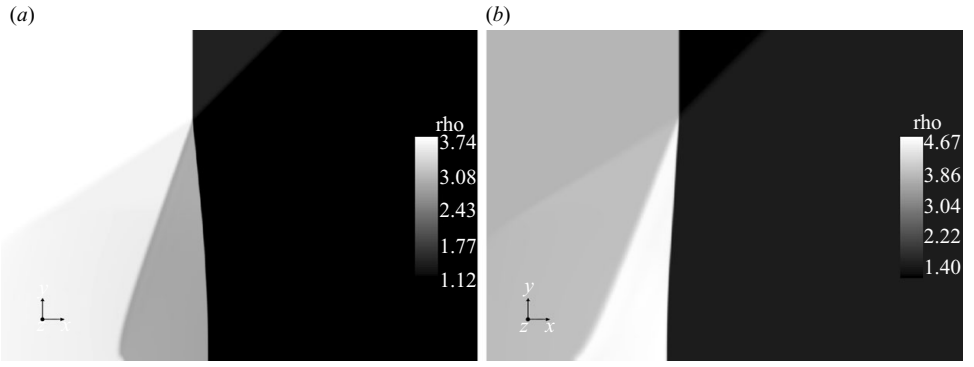

FIGURE 12. Density plots for $(\alpha, \beta^{-1}, \gamma_l, \gamma_r, M) = (\pi/4, 0, 7/5, 7/5, 2)$. (*a*) A slow–fast refraction with $\eta = 0.8$. Note that $\phi_T > \pi/2$, and R is an expansion fan. (*b*) A fast–slow refraction with $\eta = 1.2$. Note that $\phi_T < \pi/2$, and R a shock.

refraction and a reflected shock for slow–fast refraction. The transmitted signal plays a crucial role in the nature of the reflected signal: for fast–slow refraction $\phi_T < \pi/2$, but for slow–fast refraction $\phi_T > \pi/2$, and the transmitted signal bends forward. We ran our solver for varying values of M and α, and for all HD experiments with $\gamma_l = \gamma_r$, we came to the conclusion that a transition from fast–slow to slow–fast refraction coincides with a transition from a reflected shock to a reflected expansion fan, with $\phi_T = \pi/2$. This result agrees with AMRVAC simulations. In figure 12, a density plot is shown for $\eta = 1.2$ and $\eta = 0.8$.

5.6. *Effect of a perpendicular magnetic field*

In general, the MHD equations result in the following jump conditions across a CD:

$$\left[\left[\begin{array}{c} p + \dfrac{B_t^2}{2} \\ B_n \\ B_n B_t \\ v_t B_n \end{array}\right]\right] = 0. \tag{5.1}$$

It follows, that if the component B_n of the magnetic field normal to the shock front is non-vanishing, a case we did not consider so far, the MHD equations do not allow for vorticity deposition on a CD, and the RMI is suppressed (Wheatley *et al.* 2005). The remaining question is what the effect of a purely tangential magnetic field is, where the field is perpendicular to the shock front and thus acts to increase the total pressure and the according flux terms.

Also note that it follows from (3.18) and (3.19) that B/ρ is invariant across shocks and rarefaction fans. Therefore, B/ρ can only jump across the shocked and unshocked CDs, and B cannot change sign.

Revisiting the example from § 5.1, we now let the magnetic field vary. Figure 13 shows $[[v_t]](\beta)$ across the CD. Also for $\eta = 0.8$, making it a slow–fast problem, $[[v_t]](\beta)$ is shown. First notice that no shocks are possible for $\beta < 0.476$, since ω_+ would not satisfy $\omega_+ > -M$. Manipulating (3.9), we know that this is equivalent to

$$\beta > \beta_{min} \equiv \frac{2}{\gamma_l (M^2 - 1)}. \tag{5.2}$$

This relation is also equivalent to $c_1 > M$, which means that the shock is sub-magnetosonic, compared to the pre-shock region. Figure 14 shows density plots

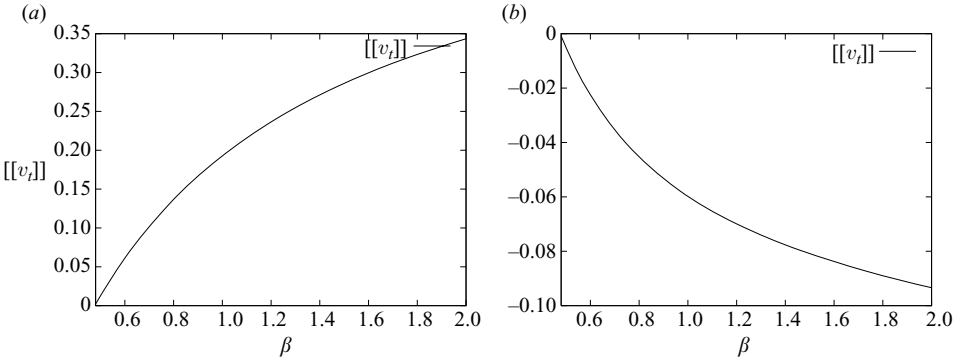

FIGURE 13. (*a*) Solution for the fast–slow problem: strong perpendicular magnetic fields decrease the instability of the CD. (*b*) Solution for the slow–fast problem: strong perpendicular magnetic fields decrease the instability of the CD.

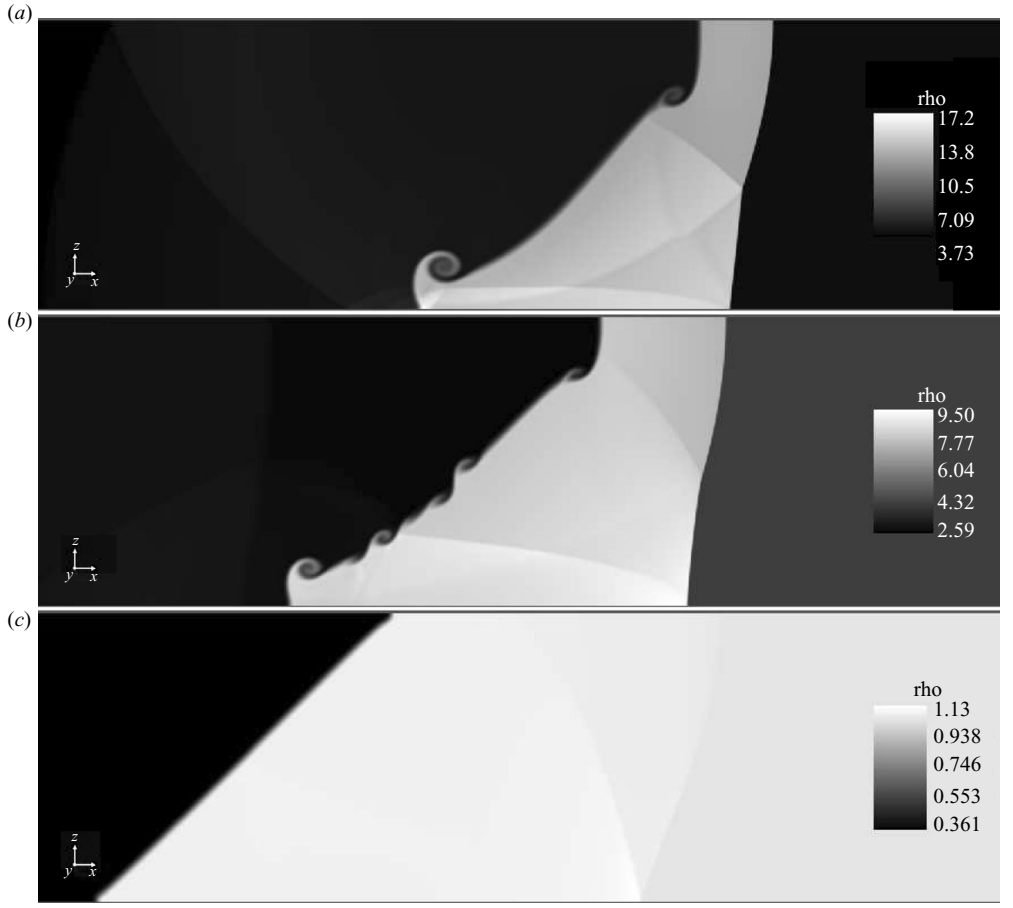

FIGURE 14. Density plots at $t = 2.0$ for $(\alpha, \gamma_l, \gamma_r, \eta, M) = (\pi/4, 7/5, 7/5, 3, 2)$ with varying β^{-1}. (*a*) $\beta^{-1} = 0$. The hydrodynamical RMI causes the interface to roll up. (*b*) $\beta^{-1} = 1/2$. Although the initial amount of vorticity deposited on the interface is smaller than in the HD case, the wall-reflected signals pass the wall vortex and interact with the CD, causing the RMI to appear. (*c*) $\beta^{-1} = 1$. The shock is very weak, and the interface remains stable.

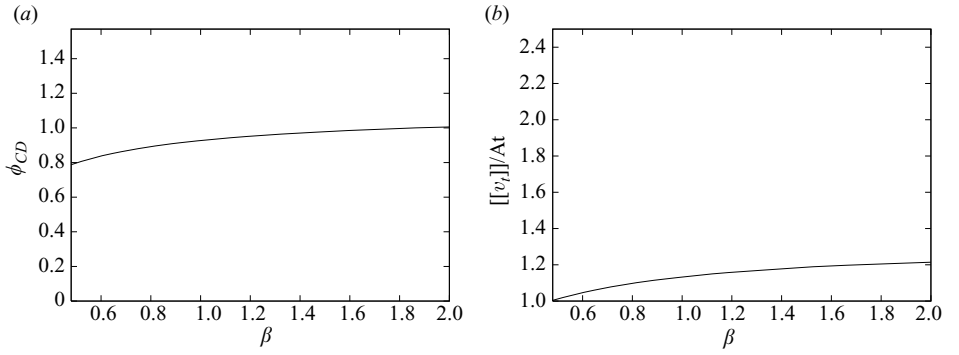

FIGURE 15. The reference problem from Samtaney (2003) with varying β. (*a*) The dependence of ϕ_{CD} on β. Note that $\lim_{\beta\to\beta_{min}} \phi_{CD} = \pi/4 = \alpha$, since this is the limit to infinitely weak shocks: $\lim_{\beta\to\beta_{min}} At = 0$. (*b*) The vorticity deposition in the shocked contact scales as the Atwood number and $\lim_{\beta\to\beta_{min}} [[v_t]]/At = 1$.

from AMRVAC simulations at $t = 2.0$, for $(\alpha, \gamma_l, \gamma_r, \eta, M) = (\pi/4, 7/5, 7/5, 3, 2)$ with varying β^{-1}. First note that the interface is instable for the HD case. Increasing β^{-1} decreases the shock strength. For β^{-1} the interface remains stable, but for $\beta^{-1} = 1$, the shock is very weak: the Atwood number $At = 0.17$, and the interface remains stable.

Shown in figure 13 is the vorticity across the CD. In the limit case of this minimal plasma-β the interface is stable, for both fast–slow and slow–fast refraction. As expected, in the fast–slow case, the reflected signal is an expansion fan, while it is a shock in the fast–slow case. Also note that the signs of the vorticity differ, causing the interface to roll up clockwise in the slow–fast regime and counterclockwise in the fast–slow regime. When decreasing the magnetic field, the vorticity on the interface increases in absolute value. This can be understood by noticing that the limit case of minimal plasma-β is also the limit case of very weak shocks. This can for example be understood by noting that $\lim_{\beta\to\beta_{min}} \phi_{CD} = \alpha$ (see figure 15). A convenient way to measure the strength of a shock is by use of its Atwood number

$$At = \frac{\rho_2 - \rho_1}{\rho_2 + \rho_1}. \tag{5.3}$$

Figure 15 shows the jump across the shocked contact $[[v_t]]$, scaled to the shock Atwood number. Note that in the limit case of very weak shocks the Atwood number equals the jump in tangential velocity across the CD, in dimensional notation:

$$\lim_{\beta\to\beta_{min}} \frac{\frac{[[v_t]]}{v_{s,1}}}{At} = 1. \tag{5.4}$$

When keeping the Atwood number constant, the shocks' sonic Mach number is given by

$$M = \frac{1 + At}{1 - At}\sqrt{\frac{(2 - 2\gamma - \gamma\beta)At^2 + (2\gamma\beta + 2\gamma)At - \gamma\beta - 2}{(\gamma^2\beta)At^2 + (\gamma^2\beta - \gamma\beta)At - \gamma\beta}} \tag{5.5}$$

$$= \sqrt{\frac{(At + 1)((\gamma\beta + 2\gamma - 2)At - (\gamma\beta + 2))}{\gamma\beta(1 - At)(\gamma At + 1)}}. \tag{5.6}$$

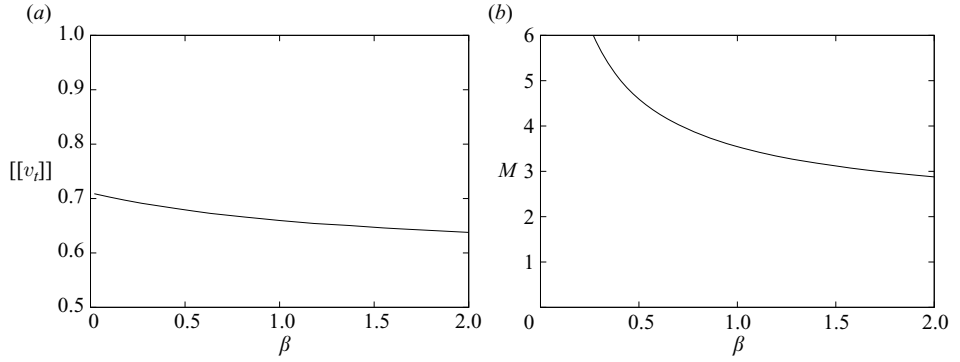

FIGURE 16. (*a*) Solution for the fast–slow problem: strong perpendicular magnetic fields decrease the instability of the CD. (*b*) Solution for the slow–fast problem: strong perpendicular magnetic fields decrease the instability of the CD.

FIGURE 17. AMRVAC plots of B/ρ for $At = 5/11$, with varying beta. (*a*) $\beta = 16$; (*b*) $\beta = 0.25$.

Note that in the limit for weak shocks

$$\lim_{At \to 0} M = \sqrt{\frac{\gamma\beta + 2}{\gamma\beta}}, \tag{5.7}$$

which is equivalent to (5.2), and in the limit for strong shocks, $M \to \infty$. Figure 16 shows the deposition of vorticity on the shocked contact, for a constant Atwood number. We conclude that under constant Atwood number, the effect of a perpendicular magnetic field is small: stronger perpendicular magnetic field increases the deposition of vorticity on the shocked contact slightly. This is confirmed by AMRVAC simulations (see figure 17).

6. Conclusions

We developed an exact Riemann-solver-based solution strategy for shock refraction at an inclined density discontinuity. Our self-similar solutions agree with the early stages of nonlinear AMRVAC simulations. We predict the critical angle α_{crit} for regular refraction, and the results fit with numerical and experimental results. Our solution strategy is complementary to the von Neumann theory and can be used to predict full solutions of refraction experiments, and we have shown various transitions possible through specific parameter variations. For perpendicular fields, the stability of the contact decreases slightly with decreasing β under constant Atwood number. We will generalize our results for arbitrary uniform magnetic fields, where up to seven signals arise. In this case we will search for non-evolutionary solutions, involving intermediate shocks, and for alternative evolutionary solutions, where the appearance of intermediate shocks can be avoided by including compound waves. We will investigate shock refraction involving initial slow, intermediate and fast shocks and qualify the effect on the refraction.

The K.U.Leuven high-performance computing cluster VIC has been used for all numerical simulations in this work.

REFERENCES

Abd-El-Fattah, A. M. & Henderson, L. F. 1978*a* Shock waves at a fast–slow gas interface. *J. Fluid Mech.* **86**, 15–32.

Abd-El-Fattah, A. M. & Henderson, L. F. 1978*b* Shock waves at a slow–fast gas interface. *J. Fluid Mech.* **89**, 79–95.

Barmin, A. A., Kulikovskiy, A. G. & Pogorelov, N. V. 1996 Shock-capturing approach and nonevolutionary solutions in magnetohydrodynamics. *J. Comput. Phys.* **126**, 77–90.

Brio, M. & Wu, C. C. 1988 An upwind differencing scheme for the equations of ideal magnetohydrodynamics. *J. Comput. Phys.* **75**, 400–422.

Chao, J. K., Lyu, L. H., Wu, B. H., Lazarus, A. J., Chang, T. S. & Lepping, R. P. 1993 Observation of an intermediate shock in interplanetary space. *J. Geophys. Res.* **98**, 17443–17450.

Chu, C. K. & Taussig, R. T. 1967 Numerical experiments of magnetohydrodynamic shocks and the stability of switch-on shocks. *Phys. Fluids* **10**, 249–256.

De Sterck, H., Low, B. C. & Poedts, S. 1998 Complex magnetohydrodynamic bow shock topology in field-aligned low-β flow around a perfectly conducting cylinder. *Phys. Plasmas* **11**, 4015–4027.

Falle, S. A. E. G. & Komissarov, S. S. 1997 On the existence of intermediate shocks. *Mon. Not. R. Astron. Soc.* **123**, 265–277.

Falle, S. A. E. G. & Komissarov, S. S. 2001 On the inadmissibility of non-evolutionary shocks. *J. Plasma Phys.* **65**, 29–58.

Feng, H. & Wang, J. M. 2008 Observations of a $2 \rightarrow 3$ type interplanetary intermediate shock. *Solar Phys.* **247**, 195–201.

Goedbloed, H. & Poedts, S. 2004 *Principles of Magnetohydrodynamics with Applications to Laboratory and Astrophysical Plasmas*. Cambridge University Press.

Hawley, J. F. & Zabusky, N. J. 1989 Vortex paradigm for shock-accelerated density-stratified interfaces. *Phys. Rev. Lett.* **63**, 1241–1245.

Henderson, R. F. 1966 The refraction of a plane shock wave at a gas interface. *J. Fluid Mech.* **26**, 607–637.

Henderson, R. F. 1991 On the refraction of shock waves at a slow–fast gas interface. *J. Fluid Mech.* **224**, 1–27.

van der Holst, B. & Keppens, R. 2007 Hybrid block-AMR in Cartesian and curvilinear coordinates: MHD applications. *J. Comput. Phys.* **26**, 925–946.

Jahn, R. G. 1956 The refraction of shock waves at a gaseous interface. *J. Comput. Phys.* **1**, 457–489.

Keppens, R., Nool, M., Tóth, G. & Goedbloed, H. 2003 Adaptive mesh refinement for conservative systems: multi-dimensional efficiency evaluation. *J. Comput. Phys.* **153**, 317–339.

Kifonidis, K., Plewa, T., Scheck, L., Janka, H.-Th. & Müller, E. 2006 Nonspherical core collapse supernovae. *Astron. Astrophys.* **453**, 661–678.

Lax, P. D. 1957 Hyperbolic system of conservation laws. Part 2. *Comm. Pure Appl. Math.* **10**, 537–566.

Meshkov, E. E. 1969 Instability of the interface of two gases accelerated by a shock wave. *Fluid Dyn.* **4**, 101–104.

Mulder, W., Osher, S. & Sethian, J. A. 1992 Computing interface motion in compressible gas dynamics. *J. Comput. Phys.* **100**, 209–228.

Myong, R. S. & Roe, P. L. 1997*a* Shock waves and rarefaction waves in magnetohydrodynamics. Part 1. A model system. *J. Plasma Phys.* **58**, 485.

Myong, R. S. & Roe, P. L. 1997*b* Shock waves and rarefaction waves in magnetohydrodynamics. Part 2. The MHD system. *J. Plasma Phys.* **58**, 521.

von Neumann, J. 1963 *Collected Works*, vol. 6. Permagon.

Nouragliev, R. R., Sushchikh, S. Y., Dinh, T. N. & Theofanous, T. G. 2005 Shock wave refraction patterns at interfaces. *Intl J. Multiphase Flow* **31**, 969–995.

Oron, D., Sadot, O., Srebro, Y., Rikanati, A., Yedvab, Y., Alon, U., Erez, L., Erez, G., Bendor, G., Levin, L. A., Ofer, D. & Shvarts, D. 1999 Studies in the nonlinear evolution of the Rayleigh–Taylor and Richtmyer–Meshkov instabilities and their role in inertial confinement fusion. *Laser Part. Beams* **17**, 465–475.

Richtmyer, R. D. 1960 Taylor instability in shock acceleration of compressible fluids. *Comm. Pure Appl. Math.* **13**, 297–319.

Samtaney, R. 2003 Suppression of the Richtmyer–Meshkov instability in the presence of a magnetic field. *Phys. Fluids* **15**, L53–L56.

Samtaney, R., Ray, J. & Zabusky, N. J. 1998 Baroclinic circulation generation on shock accelerated slow/fast gas interfaces. *Phys. Fluids* **10**, 1217–1230.

Sturtevant, B. 1987 *Shock Tubes and Waves*. VCH Verlag.

Taub, A. H. 1947 Refraction of plane shock waves. *Phys. Review* **72**, 51–59.

Todd, L. 1965 Evolution of switch-on and switch-off shocks in a gas of finite electrical conductivity. *J. Fluid Mech.* **24**, 597–608.

Toro, E. F. 1999 *Riemann Solvers and Numerical Methods for Fluid Dynamics*. Springer.

Tóth, G. & Odstrčil, D. 1996 Comparison of some flux corrected transport and total variation diminishing numerical schemes for hydrodynamic and magnetohydrodynamic problems. *J. Comput. Phys.* **128** (1), 82–100.

Wheatley, V., Pullin, D. I. & Samtaney, R. 2005 Regular shock refraction at an oblique planar density interface in magnetohydrodynamics. *J. Fluid Mech.* **552**, 179–217.

Yee, H. C. 1989 A class of high-resolution explicit and implicit shock-capturing methods. *Tech Rep.* TM101088. NASA.